Editors' Suggestion

Emergence of periodic chimneys during fluidization at a coarse-fine grains interface

Camille Porceillon [1,2] Aurélien Gay [1] Alfredo Taboada [1] and Valérie Vidal [2,*]

[1] *Géosciences Montpellier, CNRS, Université de Montpellier, Université des Antilles, Place Eugène Bataillon, 34095 Montpellier, France*

[2] *Laboratoire de Physique, École Normale Supérieure de Lyon—CNRS, 46 Allée d'Italie, 69364 Lyon Cedex 7, France*

(Received 25 June 2025; accepted 11 December 2025; published 15 January 2026)

In this work, we focus on the influence of an interface on liquid rise through an immersed granular bed. Based on laboratory experiments, we consider the migration of water injected at constant flow rate at the bottom center of a Hele-Shaw cell filled with two layers of grains immersed in water. The bottom layer is made of coarse grains, large enough to ensure liquid percolation without grain motion. The top layer consists of a bidisperse medium of fine grains and dusts about four times smaller in diameter, which can penetrate the interface between coarse and fine grains. When the liquid invades the cell, above a critical flow rate, the dusts are washed out of the coarse grains, a process called elutriation. The flow pattern self-organizes, generating fluidization chimneys at the interface between coarse and fine grains with regular spatial distribution. A model based on pressure-drop estimations predicts the pattern wavelength, which depends on the dust size and the number of coarse grains in the cell gap.

DOI: 10.1103/2m8d-7h3j

I. INTRODUCTION

Fluid migration in granular media plays a key role in natural and industrial processes such as, among others, deep-sea seepage [1,2], volcanism [3,4], volcaniclastic kimberlites [5], spouted beds [6], and catalysis [7]. These different contexts share a common observation: fluid ascent in sedimentary basins, crustal rocks, or immersed catalysts often leads to flow focusing and the formation of piercement structures [8], referred to as chimneys [9], pipes [10–12], vents [13,14], or spout channels [15], depending on the scientific community. Fundamental studies have quantified the fluid invasion regimes under either homogeneous or localized injection of liquid from below into a immersed granular bed [9,13,16–19]. At low injection rates, the fluid percolates through the granular matrix without moving the particles significantly (percolation regime). At intermediate flow rates, a stable fluid cavity forms and is either stable in time or may reach the top of the bed (fluidized cavity regime). Finally, at high injection rates, a chimney forms directly (fluidized chimney regime). Note that, when dealing with three-phase flows (e.g., gas injection in liquid-saturated sands) or cohesive particles, an additional fracturing regime appears [20–25]. In the following, only two-phase flows and noncohesive particles will be considered.

Under localized fluid injection, the critical fluidization velocity and the resulting invasion pattern in a single layer of monodisperse or polydisperse particles have been the topic of many studies [3,26–30]. They have pointed out specific structures such as elongated pipes, chimneys, or fluidized cones. In geophysical applications, however, the fluid crosses many interfaces, generated by successive sediments deposits [31]. These interfaces between particle layers of different properties, such as granulometry, may play an important role in the morphology and dynamics of pipes. Nevertheless, to our knowledge, only a few studies have focused on fluid ascent through multilayered sediments, either experimentally or numerically [12,22,32,33]. When considering the effect of an interface between coarse and fine grains, experimenters have either investigated the stable (fine on top of coarse grains) [12,22] or unstable fluidization (coarse on top of fine grains) [32]. Unstable fluidization leads to a fluidization of both the coarse and fine grain layers, while stable fluidization exhibits either a fluidization of the top fine grains only or a fluidization of both layers, depending on the injection flow rate and the relative height of both granular layers [12]. A numerical approach has pointed out that, in a given range of parameters, focused fluid-flow structures could appear at the interface between coarse and fine grains, leading to the generation of a quasiperiodic fluidization pattern [33].

In this experimental work, we investigate a bilayered water-saturated sediment composed of coarse grains overlain by a layer of fine grains. Grains are gently poured in the cell to mimic particle sedimentation in natural environments, resulting in loosely consolidated sedimentary layers. Water is injected locally at the base of the cell, in a range of flow rates such that the coarse grains are not mobilized and fine grains fluidize. The originality of this work lies in the presence of dusts in the fine grains, which can partially penetrate the coarse grain layer. Differential transport leads to the formation of quasiperiodic chimneys at the coarse-fine grains interface. In the following, we present the experiments and analysis (Sec. II). Then we characterize the pattern wavelength (Sec. III). Finally, we propose a mechanism at the origin of the formation of the quasiperiodic fluidization pattern (Sec. V).

II. MATERIALS AND METHODS

A. Experimental setup

The experimental setup consists of two superimposed sediment layers (coarse at the bottom, height h_c, and fine at the top, height h_f) fully immersed in distilled water

*Contact author: valerie.vidal@ens-lyon.fr

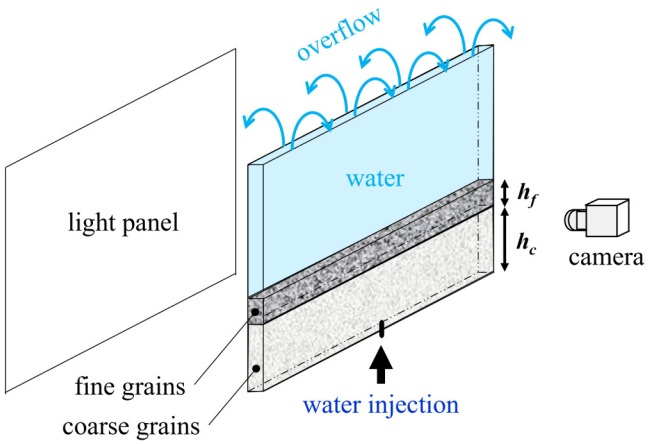

FIG. 1. Experimental setup. Water is injected at constant flow rate Q at the bottom center of a Hele-Shaw cell filled with a coarse grain layer (height h_c) topped by a fine grain layer (height h_f), fully immersed in water.

in a confined environment (Hele-Shaw cell, Fig. 1). The cell is made of two glass plates of height $H = 30.0 \pm 0.1$ cm and width $W = 35.0 \pm 0.1$ cm. To investigate the influence of confinement, two different gaps have been used, $e = 2.35 \pm 0.02$ mm and 4.12 ± 0.04 mm. A cylindrical nozzle (inner diameter 1.1 mm) at the bottom center of the cell makes it possible to inject water from below (black arrow, Fig. 1). At time $t = 0$, water is injected at constant flow rate Q by means of a pump (Tuthill 7.11.468) coupled to a flow controller (Bronkhorst mini CORI-FLOW M14-AAD-22-0-S). The range of flow rates accessible with this setup is $Q = [2–100]$ mL/min. In some experiments, the injected water (density $\rho_w = 1000$ kg m^{-3}, viscosity $\eta_w = 10^{-3}$ Pa s) is dyed dark blue (Meilleur du Chef E133, 1.2% vv.) so that the liquid entering the coarse grain layer can be visualized. Measurements show that adding dye does not affect the physical properties of the liquid. The top of the cell is left open to allow the water to spill uniformly and thus ensure a constant total height H. The spilled water is then collected using a gully surrounding the top of the cell (not shown in Fig. 1).

Although the grains are opaque (see Sec. II B), the Hele-Shaw configuration makes it possible to directly visualize the fluid migration patterns through the layers of sediments. To do so, a homogeneous light panel (Just Norm-licht Classic Line) is located behind the cell. The transmitted light is recorded with a camera (Basler monochrome, acA2040-90 µm, 2048 × 2048 pixel) mounted with a 16 mm lens and facing the cell at a distance of about 37 cm (Fig. 1). The acquisition frequency is set between 10 and 50 fps depending on the experiments, with a total recording duration between 2 and 5 minutes. Experiments are performed at room temperature. Before each experiment, a calibration grid is located inside the cell gap and a picture is taken to ensure a precise pixel/mm conversion.

B. Granular media

The grains are spherical glass beads of density $\rho_g = 2425$ kg m^{-3}. The bottom layer is composed of coarse grains (height h_c, typical diameter d_c), and the top layer is composed of fine grains (height h_f, typical diameter d_f). *Coarse* and *fine* grains are chosen so that, in the range of flow rate explored in the experiments, a monolayer of coarse grains always exhibits fluid percolation, without any significant rearrangement of the granular matrix, while a monolayer of fine grains always displays fluidization.

TABLE I. Batches of fine and coarse grains used in this work. The numbers in the Type column indicate the particle diameter or diameter range in µm as provided by the manufacturer. The median and standard deviation for the coarse grain diameter d_c and fine grain diameter d_f are reported, with the presence of dusts in the fine grain batches (median diameter d_d, see text).

	Type	d_f (µm)	d_d (µm)
Fine grains	USF Matrasur 106–212	150 ± 19	43 ± 18
	Sigmund-Lindner 100–200	165 ± 17	36 ± 19
	Type	d_c (µm)	d_d (µm)
Coarse grains	Sigmund-Lindner 400	331 ± 98	–
	Sigmund-Lindner 700	750 ± 37	–
	Dutscher 1000	1156 ± 87	–
	Prolabo 1500	1486 ± 26	–
	Dutscher 2000	2075 ± 41	–

To investigate the impact of the grain size on the fluid migration pattern, several grain batches have been used (Table I). Fine grains have a typical diameter of about 150 µm, while coarse grains are varied between 300 and 2000 µm, typically. All batches are polydisperse to prevent crystalline structures but exhibit a peaked distribution. The particle size distribution has been measured with a macroscope (Wild Makroscop M420 1.25× with Makrozoom Leica 1:5 lens). Figure 2 displays examples of particle size distributions for the two grains batches that have been used most in the experiments. Coarse grain batches exhibit similar peaked distributions [Fig. 2(b) and picture in inset], making it possible to compute a typical coarse grain diameter d_c. The originality of this work is that the fine grain size distribution is twofold [Fig. 2(a)], with fine grains of diameter d_f as provided in the supplier datasheet (right peak) and an additional peak of very fine spherical particles, henceforth named *dusts*. These dusts are clearly seen in the inset of Fig. 2(a). Their diameter $d_d \sim 40$ µm is obtained from the left peak on the distribution. Note that, although these dusts are many, due to their small size, they represent a very small amount of volume, about 4% of the total volume of grains in the topmost layer. Table I details for each grain batch used in this work, the median value and standard deviation of the coarse grain diameter d_c, the fine grain diameter d_f, and the dust diameter d_d.

C. Protocol

To ensure reproducible experiments, we use the following protocol. First, the cell is partially filled with distilled water (height ∼10 cm). The coarse grains are then gently poured through the top aperture, uniformly along the cell width, to form the bottom layer. This layer is leveled delicately with a thin ruler to achieve a horizontal surface while avoiding grain compaction. The coarse grain layer is thus set at height h_c. We then repeat the same process of sedimentation and

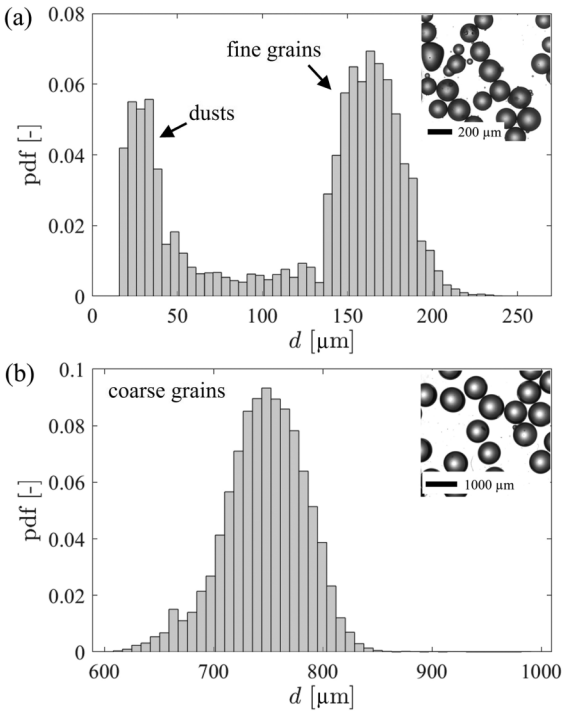

FIG. 2. Particle size distribution (probability density function, pdf) showing the diameter d for a measurement over N particles, for the two grain batches most used in the experiments. (a) Fine grains Sigmund-Lindner 100–200 ($N = 8781$). (b) Coarse grains Sigmund-Lindner 700 ($N = 10211$). All batches (Table I) exhibit similar distributions, with a median coarse grain diameter d_c [here, 750 µm, see (b)], a median fine grain diameter d_f corresponding to the right peak in (a) [here, 165 µm], and the additional presence of very fine grains or dust, with a median diameter d_d corresponding to the left peak in (a). Insets: Pictures showing the coarse grains (b) and both fine grains and dusts (a).

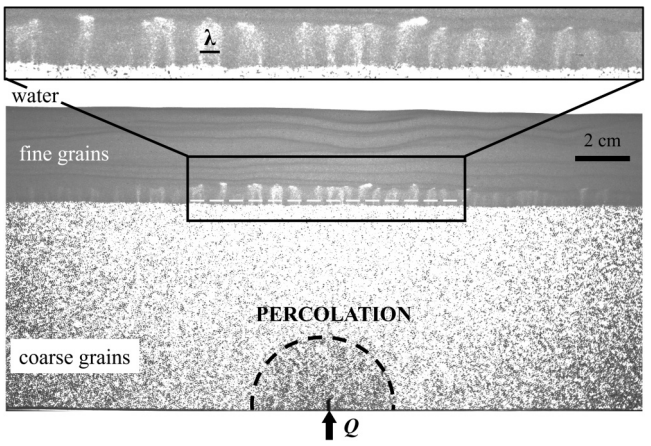

FIG. 3. (bottom) Snapshot of a typical experiment showing the percolation front in the coarse grains (dyed region, black dashed line) and the simultaneous emergence of a periodic fluidization pattern at the coarse-fine grains interface, mostly seen at the cell center (black rectangle). The white dashed line is used for intensity analysis, see text. (top) Zoom on the central region. λ indicates the characteristic distance between two neighboring chimneys at the interface ($e = 2.35$ mm, $d_c = 750$ µm, $h_c = 8$ cm, $d_f = 150$ µm, $h_f = 3$ cm, and $Q = 50$ mL/min).

leveling for the fine grain layer (height h_f). As the fine grain distribution is bidisperse [Fig. 2(a)], segregation may occur during pouring and sedimentation. To minimize this effect, we slowly pour small amounts of the fine grains back and forth along the cell width and accumulate successive layers until reaching the height h_f. The water level above the grains is topped up until the fluid overflows (Fig. 1). At time $t = 0$, water is injected at constant flow rate Q, and the experiment starts. This protocol is repeated for each set of experimental parameters (d_c, h_c, d_f, h_f, Q, and e), except when varying h_f (see Sec. III D).

D. First observations and image analysis

Figure 3 (bottom) displays the snapshot of a typical experiment a short time after the fluid injection at the bottom. As the injected water is dyed in this experiment, we observe the incoming fluid percolating through the coarse grain layer (dark semicircled region at the cell bottom; the dashed black line highlights the percolation front). We remind here that both coarse and fine grains are fully immersed in water. As this fluid is incompressible, the injected fluid does not only invade the cell bottom around the injection nozzle but simultaneously pushes the surrounding fluid upward throughout the system. The water overflow, not shown in Fig. 3, is indeed observed right after the beginning of the fluid injection. As stated in Sec. II B, the coarse grains are chosen so that the fluid will always percolate through them in the range of flow rates explored in this work. Conversely, the fine grains, as a monolayer, always fluidize in the same range of flow rate. For the bilayered experiment, we expect percolation in the coarse grain layer, and either percolation in the topmost, fine grain layer or, at higher flow rate, fluidization of these fine grains.

Interestingly, in a given range of parameters, we report a regular, quasiperiodic fluidization pattern occurring in the fine grains, right above the interface. Movie 1 in the Supplemental Material [34] shows a typical example of the formation of this pattern for $e = 2.35$ mm, $d_c = 750$ µm, $h_c = 8$ cm, $d_f = 165$ µm, $h_f = 3$ cm, and an injection flow rate $Q = 30$ mL/min; and Movie 2 in the Supplemental Material [34] displays the same experiment with a zoom on the interface. These supplemental movies have been specifically acquired to illustrate the phenomenon, with an additional color camera (Basler acA2040-90um, 2048 × 2048 pixels, 25 mm lens) to image the whole cell and the black and white camera used in all other experiments (see Sec. II A) equipped with a 75 mm lens, both cameras being located at about 85 cm from the cell. The pattern consists of small fluidization chimneys or pipes, regularly spaced along the coarse-fine grains interface. These chimneys locally focus the fluid flow and act as secondary sources at the interface. As the injected water is colored with blue dye (Movie 1 in the Supplemental Material [34]), it points out that the chimneys appear after a short transient and much before the blue liquid reaches the interface. In the zoomed Movie 2 in the Supplemental Material [34], we can see that, as soon as the injection starts ($t = 0$ at the beginning of both movies), motion is observed in the coarse grain layer right below the interface, while the coarse grains themselves remain motion-

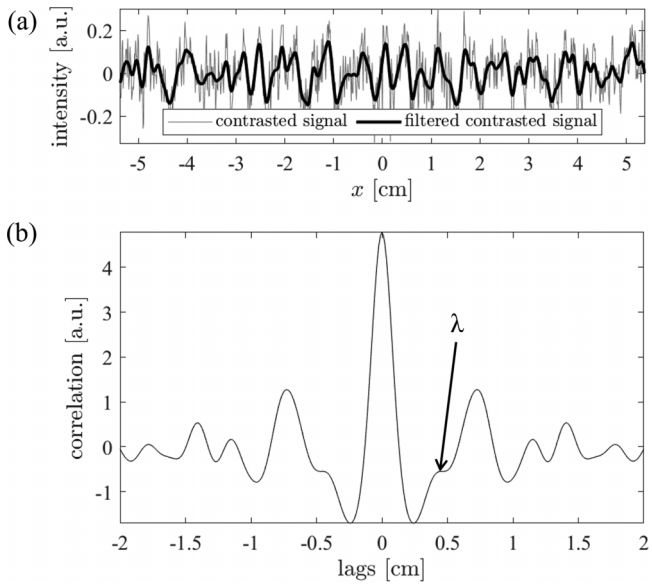

FIG. 4. (a) Light intensity profile along the horizontal white dashed line in Fig. 3 after image contrast enhancement and background removal (thin gray line). The thick black line corresponds to low-pass filtering to remove the noise. Note the quasiperiodicity of the intensity pattern. x is the horizontal coordinate, with $x = 0$ at the vertical of the injection nozzle. (b) Autocorrelation function of the filtered intensity profile [thick black line in (a)]. The first peak indicates the typical distance λ between two fluidization chimneys at the interface.

less. This observation hints toward the crucial role of dusts, which have penetrated the coarse grain layer (see discussion in Secs. IV A and IV B). Note that the chimneys stay at the same location and do not evolve significantly in time, until the fine grain layer is fully fluidized and the experiment stops. In the following, we will quantify this instability, which is characterized by a typical distance λ between two fluidization chimneys at the interface.

Image processing enables the extraction of the light intensity profile along a line right above the interface (white dashed line, Fig. 3). After image contrast enhancement (adapthisteq, Matlab) and background removal, the signal is low-pass filtered to remove the noise [Fig. 4(a), black line]. The quasiperiodicity of the intensity pattern clearly appears, with a characteristic distance λ. To quantify λ, the autocorrelation of the signal is performed, as shown in Fig. 4(b). It displays, as expected, a large peak for a zero lag, followed by secondary peaks indicating the presence of a quasiperiodic pattern. The first peak or shoulder is chosen for the quantification of λ [black arrow, Fig. 4(b)]. Note that it is not necessarily the largest secondary peak. Indeed, the fluidization pattern, although quasiperiodic, is not fully regular. The chimneys formed at the interface are mostly separated by a distance λ, but due to heterogeneities in the medium, a chimney may not form sometimes, and the distance between two neighboring pipes thus increases up to 2λ, as seen in Fig. 3, top. This source skipping impedes determining λ by a simple peak average distance in the intensity signal [Fig. 4(a)]. Although the chosen peak in the correlation function can be challenging to identify, it has been manually checked on several series that it is the most representative of the regular fluidization pattern, as displayed in Fig. 3. For each experiment, this analysis is performed on 30 images right after the onset of the instability. In the following, each λ is taken as the median value of these 30 measurements, and the associated error bar is the corresponding standard deviation.

III. RESULTS

A. Dependence on the injection flow rate Q

Varying the injection flow rate Q changes the injected fluid velocity in the granular matrix. As we focus on the formation of a fluidization pattern at the coarse-fine grains interface and use experimental cells with a different gap e, the physically relevant parameter is the fluid velocity v_i at the interface. As we locally inject the fluid at the bottom center of the cell, $v_i(x)$ varies along the interface, with its maximum value at the vertical of the injection nozzle. However, assuming a radial field for the fluid velocity during the percolation process, this variation is small in the central region, where the fluidization pattern forms. Note that, in this central region, the chimneys associated with the secondary sources form roughly simultaneously.

In the following, we approximate in the central region $v_i(x) \simeq v_i(0) = v_i$. This quantity is obtained by fluid mass conservation, with the assumption of a radial fluid velocity field in the coarse grain layer

$$v_i = \frac{Q}{\pi \varepsilon h_c e}, \tag{1}$$

where h_c is the coarse grain layer height, $\varepsilon = 1 - \phi_c$ its porosity, and ϕ_c its packing fraction. Due to the polydisperse coarse grain distribution [Fig. 2(b)], this porosity cannot be predicted. It has been computed for each experiment by measuring the mass m_c of coarse grains needed to reach the height h_c:

$$\varepsilon = 1 - \frac{m_c}{\rho_g V_c}, \tag{2}$$

where $V_c = h_c e W$ is the volume of the coarse grain layer. For all experiments, the porosity is of the same order of magnitude $\varepsilon \simeq 0.4$, corresponding to loose random packing.

Figure 5 displays the typical distance λ between successive fluidization chimneys at the interface as a function of the fluid velocity v_i for different cell gaps and the two fine grain batches. Here, v_i is varied by changing the flow rate Q and the cell gap e (2.35 and 4.12 mm), at fixed $h_c = 8$ cm (see Sec. III C). We report a critical velocity $v_{ic} \simeq 1$ mm/s separating two fluid migration regimes. For $v_i < v_{ic}$, the fluid velocity is not strong enough to entrain the particles, and there is no fluidization in the topmost layer. The rising fluid percolates through both the coarse and fine granular layers (gray region, Fig. 5). For $v_i > v_{ic}$, the fluid entrains the grains directly above the interface, forming the fluidization pattern, as shown in Fig. 3. Figure 10 in the Appendix displays the dependence of λ with Q. As expected, the critical flow rate Q_c above which the fluidization pattern is observed depends on the cell gap e. For $e = 4.12$ mm, Q_c is approximately twice the value observed for $e = 2.35$ mm (respectively shown by the dark purple and light orange dashed lines in Figure 10

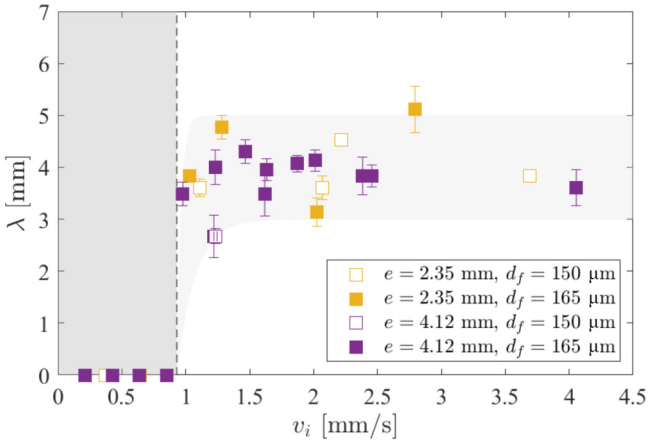

FIG. 5. Typical length λ of the fluidization pattern as a function of the fluid velocity v_i at the interface. The vertical dashed line indicates the velocity threshold $v_{ic} \simeq 1$ mm/s. For $v_i < v_{ic}$, there is no fluidization (dark gray region). For $v_i > v_{ic}$, the fluidization pattern forms independently of the cell gap e ($d_c = 750$ μm, $h_c = 8$ cm, and $h_f = 3$ cm). The light gray region is a guideline for the eye.

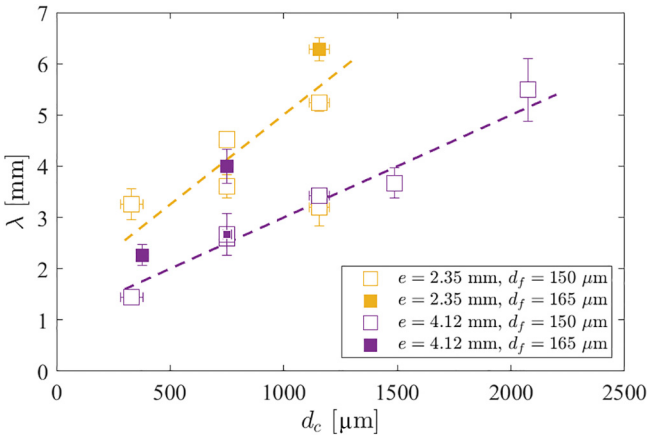

FIG. 6. Typical length λ of the fluidization pattern as a function of the coarse grain diameter d_c ($h_c = 8$ cm, $h_f = 3$ cm, and $Q = 30$ mL/min). The orange and purple dashed lines are guidelines for the eye for $e = 2.35$ and 4.12 mm, respectively. The slope ratio between these guidelines is equal to the cell gap ratio.

in the Appendix). Once the fluidization chimneys are formed at the interface, they remain stable at their location. The characteristic spacing λ is roughly independent of v_i, of the fine grain batches, and of the cell gap e (Fig. 5). It ranges from about 3 to 5 mm, about 4 to 7 times the coarse grain size. Consistently, the average distance between pipes remains roughly constant, while the vertical component of velocity decreases laterally along the interface. Note that, far from the cell center, the fluid velocity v_i at the interface may not exceed the threshold v_{ic} anymore, and fluidization should not happen. Indeed, we report from the observations, in a given range of flow rates, the absence of fluidization pattern on the cell sides (see Fig. 3).

As λ does not depend significantly on v_i or Q once the fluidization pattern is formed, in the following, unless specified, we set $Q = 30$ mL/min. The associated velocity v_i at the interface depends on the coarse grain height h_c, porosity ε, and cell gap e [Eq. (1)]. In all experiments, $h_c = 8 \pm 0.2$ cm and $\varepsilon = 0.40 \pm 0.03$, which corresponds to $v_i \simeq 1.2$–1.3 mm/s for $e = 4.12$ mm and $v_i \simeq 2.0$–2.2 mm/s for $e = 2.35$ mm.

B. Dependence on the coarse grain diameter d_c

Figure 6 displays the variation of λ with the coarse grain diameter d_c. The characteristic length of the pattern increases linearly with d_c, with a different slope depending on the cell gap e. Despite their slight difference, the two fine grain batches follow the same trend (orange and purple dashed lines, Fig. 6). Note here that the linear functions displayed as guidelines for each cell gap have a slope ratio equal to the cell gap ratio, indicating at first order a dependence of λ on d_c/e. Two points appear out of trend. First, for $e = 4.12$ mm, $d_f = 165$ μm, and $d_c = 750$ μm, the dark purple point is much above the general trend for the largest cell gap. Carefully analyzing the images shows that, in this experiment, many chimneys are skipped at the interface (see comment on the interface heterogeneity at the end of Sec. II D). The correlation function therefore gives either λ, 2λ, or an unusable result depending on the image. To be consistent with the analysis of all experiments, the value reported in Fig. 6 is the median value of all extracted wavelengths, but this value gives 2λ rather than λ. The second point out of trend is for $e = 2.35$ mm, $d_f = 150$ μm, and $d_c = 1156$ μm. In this case, two typical distances λ have been extracted from the same experiment λ = 3.2 and 5.2 mm. It was not possible to report either from the images or from the correlation function which length was the most characteristic. However, it is important to note that, for this experiment, the coarse grain size becomes of the order of the cell gap, and barely one or two coarse grains can fit in the gap. It is therefore probable that the fluidization pattern is biased by strong wall effects. The interpretation of the influence of d_c on λ will be further discussed in Sec. IV C 1.

C. Dependence on the coarse grain height h_c

We do not present here a systematic study of the fluidization pattern when varying the coarse grain layer height h_c. Indeed, the requirement for the fluidization pattern to appear at the interface is percolation in the coarse grains and fluidization in the superimposed fine grains. As pointed out in Sec. III A, the physically relevant parameter is the fluid velocity at the interface v_i. Under these conditions, varying the coarse grain layer height h_c is equivalent to varying the flow rate Q [see Eq. (1)]. In this work, we have chosen $h_c = 8$ cm so that the flow rates needed to reach and exceed the critical velocity v_{ic} to generate the fluidization pattern at the coarse-fine grains interface are in the range of the flow controller.

D. Dependence on the fine grain height h_f

In this section, we assess the dependence of λ on the fine grain height h_f. Given the time-consuming preparation of the initial bilayered condition (see Sec. II C), we adopted the following protocol for this part. Instead of preparing each experiment from an empty cell, we adjust the fine grain height between each experiment, without removing the grains from

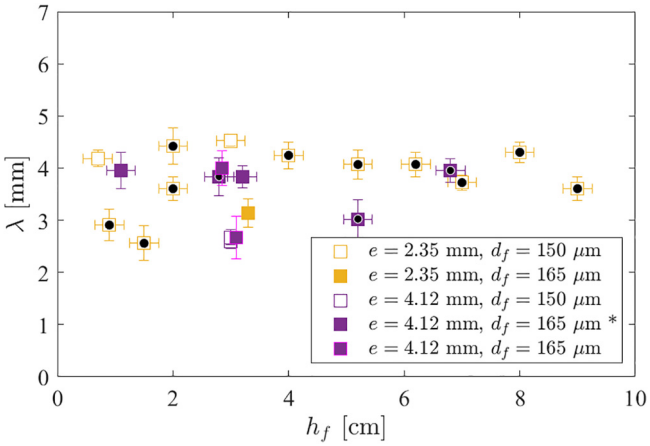

FIG. 7. Typical length λ of the fluidization pattern as a function of the fine grain height h_f ($d_c = 750$ μm, $h_c = 8$ cm, and $Q = 30$ mL/min, except *, for which $Q = 60$ mL/min). The black dots indicate experiments using the final state of the previous run as the initial condition, after allowing the particles to resettle in the cell (see text).

the previous experiment. To do so, we start from a small fine grain layer ($h_f = 0.7$ mm). After the formation of the fluidization pattern, we let the experiment run until the top, fine grain layer is fully fluidized. At this point, both the fine grains and dusts are in suspension. We then turn off the water injection and wait for particle sedimentation. After a few minutes, we then add fine grains from the top, up to the new h_f, and start the experiment again. It has been checked for a few data points that the resulting λ was independent of the initial preparation of the system by doing the same experiments from an empty cell.

The corresponding results are shown in Fig. 7. Whichever the cell gap, λ remains roughly constant when h_f increases. This result may be surprising, as we could expect the fluidization pattern to change when the confinement pressure increases. However, let us remind that the grains are confined in the transverse direction between the two glass plates of the Hele-Shaw cell. In this configuration, we expect the Janssen effet to occur [35,36], thus modifying the apparent weight of the top layer of fine grains. From the experimental results shown in Fig. 7, we can conclude that, in the range of parameters explored in this work, λ is independent of the fine grain height.

IV. DISCUSSION

A. Origin of the fluidization pattern

The coarse grains have been chosen so that the fluid percolates through the bottom layer. They remain motionless during the experiments, as confirmed by direct observations. We remind that, due to direct light transmission technique (Fig. 1), we are able to visualize grain motion not only near the front wall but throughout the entire bulk (cell gap). At the onset of the fluidization pattern, particles in the top layer, right above the interface, are entrained by the fluid. As highlighted in Sec. II B, the originality of this work lies in the effect of a bidisperse granular medium in the top layer on the emergence of a regular fluidization pattern at the coarse-fine grains interface. The presence of dusts alongside fine grains in the top layer affects the fluid transport in saturated conditions. These dusts, being the smallest particles, are more easily entrained by the ascending flow and will mobilize at a local fluid velocities lower than those required to displace the fine grains.

The typical Reynolds number associated with particle motion is given by $\mathrm{Re} = \rho_w v d/\eta_w$, where d is the particle diameter. Considering that the velocity v_i at the interface ranges between 1 and 4 mm/s, the Reynolds number range is of about [0.04–0.16] for the dusts ($d_d \sim 40$ μm) and [0.15–0.6] for the fine grains ($d_f \sim 150$ μm). In the laminar regime ($\mathrm{Re} < 1$), the particle sedimentation velocity can be approximated by the Stokes velocity

$$v^* = \frac{(\rho_g - \rho_w)}{18\eta_w} g d^2. \tag{3}$$

The sedimentation velocity is therefore $v_d^* \simeq 1.2$ mm/s for the dusts and $v_f^* \simeq 17.5$ mm/s for the fine grains. Note that v_d^* is of the same order of magnitude as the critical velocity at the interface necessary to observe the fluidization pattern $v_{ic} \simeq 1$ mm/s (Fig. 5, Sec. III A).

Here, we propose that *elutriation* is the mechanism at the origin of the fluidization pattern. Elutriation refers to the entrainment of finer particles when a fluid flows through a polydisperse granular medium, the larger particles remaining motionless [37,38]. Figure 8 illustrates the proposed mechanism. At $t = 0$, just before opening the fluid injection, particles are motionless in the bottom and top layers. Due to their small diameter, dusts partially invade the pore spaces between coarse grains beneath the interface [Fig. 8(a), left]. When fluid is injected and, owing to its incompressibility, flows through the entire system, two situations may arise. If the velocity at the interface is too small to lift any of the particles ($v_i < v_d^* < v_f^*$), the fluid percolates through both the coarse and fine grain layers and no fluidization occurs (Fig. 5, $v_i < v_{ic}$). Above a critical flow rate (or critical velocity $v_{ic} \simeq v_d^*$), the drag force counterbalances the particle weight, and the smaller particles (dusts) are entrained by the fluid, while the fine particles remain motionless [$v_d^* < v_i < v_f^*$, Fig. 8(a), center]. At this stage, dust particle distribution within the coarse grain pore network reorganizes, initiating the elutriation process. This process can be clearly seen in Movie 2 in the Supplemental Material [34], as described in Sec. II D. The local pore opening or clogging modifies the fluid flow [Fig. 8(a), right], leading to a local velocity increase (thick blue arrows) or decrease (dashed blue line), respectively. In this latter case, the local velocity can become smaller than v_d^*, stopping the dust motion. As this process repeats, the open pores elutriate more efficiently and enlarge further, capturing the neighboring fluid flow and redirecting it through these preferential pathways until flow through adjacent blocked regions ceases completely (red cross). In the open region (fraction α of the initial surface), the local velocity can increase until becoming large enough to lift the fine grains [$v_d^* < v_f^* < v_i/\alpha$, Fig. 8(a), right, thick blue arrow].

This repetitive process along the interface leads to the quasiperiodic fluidization pattern shown in Fig. 3, characterized by a typical distance λ. The sketch in Fig. 8(b) illustrates

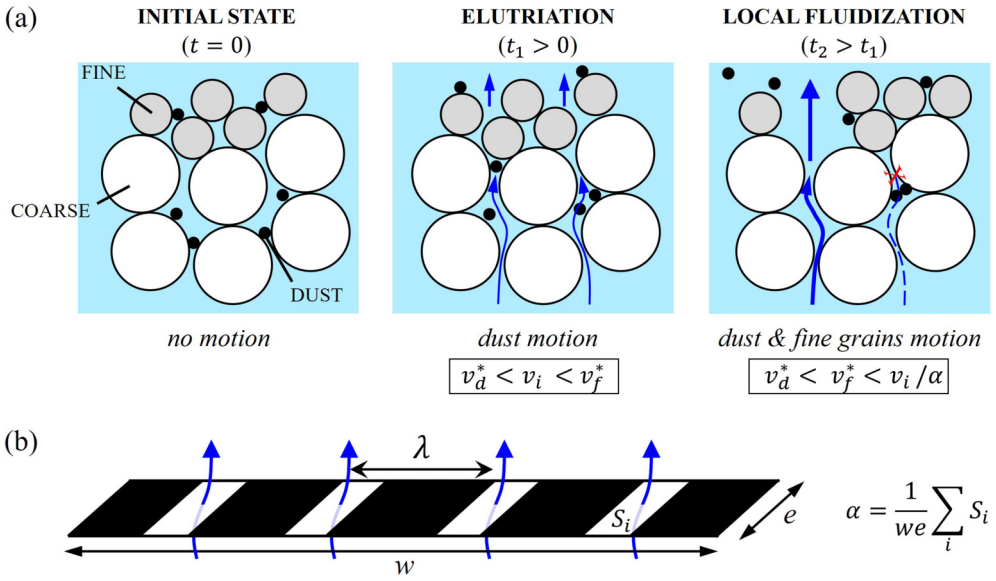

FIG. 8. (a) Illustration of the mechanism at the origin of the fluidization pattern. (left) Zoom on the coarse-fine grains interface. In the inital state ($t = 0$, no fluid flow), particles are motionless with coarse and fine grains in the bottom and top layers, respectively. Dusts partially invade the coarse grain pores. (center) For $t_1 > 0$, the fluid flow (blue arrows) can entrain the dusts ($v_i > v_d^*$) but not the fine grains ($v_i < v_d^*$). The dust distribution in the coarse grain pore network reorganizes, initiating the elutriation process. (right) For $t_2 > t_1$, dust motion creates a dynamic feedback loop: some pores widen, causing local velocity increases (thick blue arrows), while others become constricted, reducing local velocity below v_d^*, which halts dust transport in these regions. In regions where pores become constricted, fluid flow is redirected toward adjacent open pathways, eventually ceasing entirely in the blocked areas (red cross). The fluid locally crosses the interface over a smaller area (fraction α of the initial area) and can then have a velocity larger than v_f^*, entraining both the dusts and the fine grains. (b) The repetition of the local mechanism in (a) along the interface (width w), over the gap e, leads to the fluidization pattern shown in Fig. 3, characterized by λ (white regions of surface S_i, liquid flow; black regions, no liquid flow). α is defined as the fraction of the interface through which the liquid flows.

a segment of the interface (width w, surface we) showing the alternating pattern of open (white) and closed (black) regions through which the fluid flows (blue arrows) or is arrested, respectively. Note that, due to the radial velocity field, the velocity is not uniform along the interface, and the pattern may appear on the cell center only ($w < W$). The fraction α of the interface through which the fluid flows is defined as

$$\alpha = \frac{1}{we}\sum_i S_i, \tag{4}$$

where S_i is the surface of a single white region in Fig. 8(b), and the sum is computed over all the white (fluidized) regions of the fluidization pattern. The fraction α of open region at the interface can be estimated as $\alpha \simeq v_{ic}/v_f^* \sim 6\%$. Despite image processing efforts, it proves difficult to estimate α experimentally, as the region close to the interface does not appear clear enough to distinguish the exact extension of a locally fluidized region (Fig. 3, top).

From the fraction α of the interface through which the fluid flows, it is interesting to estimate the extension Δy of the chimneys in the y direction, along the cell gap. Along the interface, in the x direction, as the coarse grains do not move, the secondary sources are typically of the size of a pore $d_{p_c} = \zeta d_c$, with ζ of the order of a few percent. The surface through which the fluid flows can thus be written $\alpha we = N d_{p_c} \Delta y$, where N is the number of secondary sources or chimneys along the interface, in the central region of width w. From Fig. 3, top, we have $N \simeq 35$ and $w \simeq 5$ cm, yielding $\Delta y \simeq e$. The chimneys therefore occupy all the cell gap, as illustrated in the schematic representation of Fig. 8(b).

B. Elutriation and fluidization pattern

Although the elutriation process cannot be observed directly in our experimental setup, its significance can be readily demonstrated through the critical role of dusts. We sieved fine grain batches to remove dusts before filling the cell, and none of the experiments conducted with these cleaned batches exhibited fluidization. Without dusts, all experimental parameters being kept constant (coarse and fine grain layer height, flow rate, etc.), we have always observed percolation, not only in the coarse grain layer but also throughout the fine grain layer. The dusts are therefore essential for initiating grain motion and creating preferential pathways which subsequently lead to fine grain mobilization and the formation of a quasiperiodic fluidization pattern.

The inherent heterogeneity of granular media likely explains why the fluidization chimneys at the interface do not maintain a uniform characteristic spacing of λ between each pipe. Indeed, local variations in packing fraction, grain size distribution, and force chain networks create regions where fine particles are more or less mobile. These heterogeneities produce two observable effects: (1) small variations in the characteristic distance λ between chimneys, causing minor deviations from perfect periodicity, and (2) occasional skipping of potential fluidization sites, resulting in neighboring pipes separated by approximately 2λ. This explains why the

peak associated with the pattern wavelength is not the secondary maximum of the correlation function (see Sec. II D and Fig. 4).

C. Dependence of λ

1. Influence of the coarse grain diameter d_c

To account for the variation of λ with the coarse grain diameter (Fig. 6), we consider the following. A chimney forms at the interface if locally, a pore opens enough due to the elutriation process so that the local fluid velocity overcomes v_f^*, the critical velocity to lift a fine grain. Subsequently, this pore drains the flow from the neighboring pores over a typical distance λ. As a first crude approximation, we consider that the medium is homogeneous and that the flow is equally distributed along the interface with a local vertical flow rate Q_i through each coarse grain pore. The pressure drop due to pore opening in the coarse grains directly beneath the interface can be written from Darcy's law

$$\delta P_z = \frac{128\eta}{\pi} L_z \left(\frac{Q_i}{d_{p_{\text{init}}}^4} - \frac{Q_i}{d_{p_{\text{end}}}^4} \right), \tag{5}$$

where $L_z = N_z d_c$ is the typical vertical distance over which this pressure drop occurs, N_z being the number of coarse grains below the interface which have been elutriated from dusts and locally focus the vertical fluid flow. Here, $d_{p_{\text{init}}}$ and $d_{p_{\text{end}}}$ are the coarse grains pore diameter before ($d_{p_{\text{init}}}$) and after ($d_{p_{\text{end}}}$) the elutriation process. They can be estimated as $d_{p_{\text{init}}} \simeq d_{p_c} - d_d$ (pore filled with a dust particle) and $d_{p_{\text{end}}} \simeq d_{p_c}$ (fully open pore), with d_{p_c} the coarse grain typical pore size. Rewriting Eq. (5) gives

$$\delta P_z = \frac{128\eta N_z d_c}{\pi} \frac{Q_i}{d_{p_c}^4} \left[\frac{1}{\left(1 - d_d/d_{p_c}\right)^4} - 1 \right]. \tag{6}$$

This pressure drop must be compared with the horizontal pressure drop necessary to drain the flow from the neighboring pores in the (x, y) horizontal plane, as represented in Fig. 9(a):

$$\delta P_x = \frac{128\eta}{\pi d_{p_c}^4} \left(\frac{\lambda}{2} \right) N_y Q_i \,, \tag{7}$$

where $N_y \simeq e/d_c$ is the number of pores along the gap, in the y direction. When the secondary source initiates, $\delta P_z \sim \delta P_x$. Assuming $d_d \ll d_{p_c}$ and $d_{p_c} = \zeta d_c$ (see Sec. IV A) leads to

$$\lambda \sim \xi d_d \left(\frac{e}{d_c} \right)^{-1}, \tag{8}$$

with $\xi = 8N_z/\zeta$. In the following, we consider $\zeta \simeq 10\%$.

Figure 9(b) displays the normalized pattern wavelength λ/d_d as a function of e/d_c. The data are the same as in Fig. 6, but we choose here to plot the normalized wavelength as a function of e/d_c rather than d_c/e, as $N_y \simeq e/d_c$ represents the typical number of grains or pores in the gap (see above) and is physically more relevant. The colored lines show the prediction from Eq. (8) when varying the number of coarse grains in the z direction N_z over which elutriation occurs. Without any adjustable parameters and despite the crude approximations, the model captures well the order of magnitude and variation

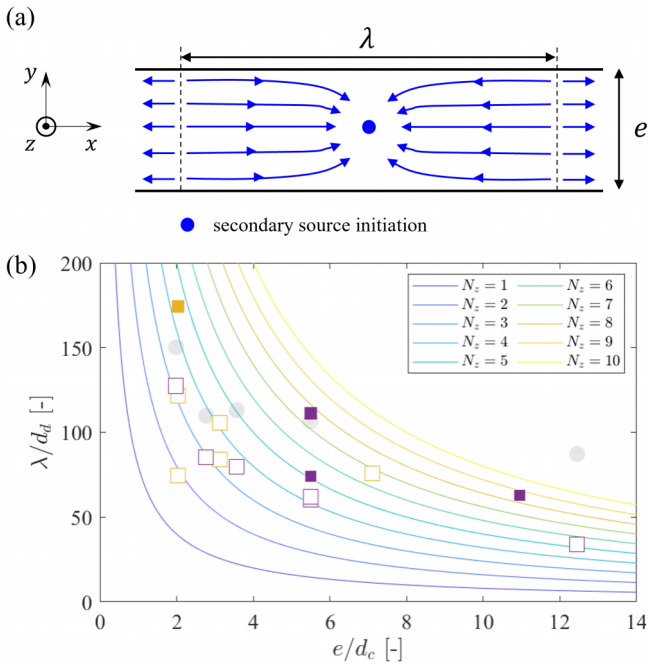

FIG. 9. (a) Sketch representing the flow pattern in the (x, y) horizontal plane. When a pore opens at the interface due to the elutriation process (blue dot), it drains the adjacent pore flow over a length λ. (b) Characteristic length λ of the fluidization pattern normalized by the dust diameter d_d as a function of (e/d_c) (same legend as Fig. 6). The light gray dots indicate the series with $Q = 60$ mL/min, far from the pattern initiation threshold. The colored lines indicate the prediction from Eq. (8), with the number of coarse grains N_z which have been elutriated in the z direction indicated in the legend.

of the experimental data. It predicts $N_z \sim 3$–5, which is physically relevant, as we expect the dusts to penetrate over a few coarse grain layers and, thus, the elutriation process to take place over this length scale.

For a higher flow rate, the model prediction stands fairly well [$Q = 60$ mL/min, gray dots, Fig. 6(b)]. In this case, however, the interpretation must be made with caution. Indeed, the above model only stands at the chimney initiation threshold and may fail for higher flow rates. Finally, note that the model relies on strong hypotheses, in particular that the number of coarse grains over which the elutriation process occurs N_z is constant. However, N_z could possibly depend on the coarse grain diameter d_c, as larger pores could lead to deeper penetration of the dusts into the coarse grain layer. Conversely, a higher coarse grain polydispersity would lead to a shallower penetration and a smaller value of N_z. This could explain part of the data scattering in Fig. 6(b).

2. Influence of the fine grain and dust diameters (d_f, d_d)

Varying the fine grain diameter d_f and dust diameter d_d over a large range is difficult in our experiments. Indeed, the bidisperse size distribution of the top layer is crucial to observe the fluidization pattern, which is triggered by the elutriation process described in Sec. IV A. If we consider smaller fine grains, there is no more difference between fine grains and dusts, and the successive motion of dusts and fine grains cannot be observed. Considering larger particles, on

the contrary, increases their Stokes velocity and therefore the critical fluid velocity necessary to initiate fluidization. Higher flow rates should be fixed to reach these velocities, which is not accessible in the range of the pump or which would lead to both the coarse and fine grain layer fluidization.

D. Instabilities and flow localization

The above results can be discussed in the broader context of instabilities generation at an interface and flow localization.

Since the pioneering work of Saffman and Taylor and the so-called Saffman-Taylor instability at the interface between two nonmiscible viscous fluids [39], the emergence and growth of instabilities at the interface between two nonmiscible viscous fluids have been widely studied. This so-called Saffman-Taylor or viscous fingering instability is observed when a less viscous fluid invades a more viscous fluid under a pressure gradient within a confined geometry, such as a porous medium or a Hele-Shaw cell. Without forced fluid injection, gravity-driven instabilities may also emerge at the interface between two fluids of different densities. Unstable conditions in this case arise when the heavier fluid is above the lighter one, leading to the so-called Rayleigh-Taylor instability [40,41]. More recent works have emphasized the generation of fingering instabilities when injecting a fluid into a saturated granular medium (see Refs. [42–48] and references therein). Only a few studies, however, have focused on the emergence of instabilities at a granular interface.

In a numerical study, Yarushina *et al.* [33] demonstrated that porosity-dependent permeability at an interface could trigger the development of localized flow channels. This recent work has been performed in the framework of fluid-escape pipes and geohazard prediction for petroleum and CO_2 storage sites [33]. A similar phenomenon of flow localization at a coarse-fine grains interface has been reported and widely studied in the engineering community in the context of erosion in layered soils. Soil contact erosion occurs at the interface between coarse and fine grain layers submitted to a flow parallel to the interface. Above a critical flow velocity, entrainment of fine particles through the coarse grain pores leads to flow localization and subsequent erosion, with dramatic consequences for dam or dyke safety [49–51]. However, these previous works mostly focused on the triggering of a (single) localized flow. Only the simulations of Yarushina *et al.* [33] mention the possible appearance of regular fluidization chimneys at the interface. The formation of such quasiperiodic flow localization has been pointed out in the absence of an interface, when a liquid flows through a bidisperse granular medium [27]. In that case, internal erosion and channelization occur, leading to regular preferential pathways, observed both experimentally and numerically. The underlying mechanism is the same as previously described, with smaller grains being entrained through the larger grain pores [27].

In this work, we show experimental evidence of quasiperiodic instabilities and the formation of a regular fluidization pattern at a coarse-fine grains interface. The crucial role of dusts invading the coarse grain pores leads the system to face filtration issues such as pore clogging, selective particle retention, and flow path modification [50–54], enhancing the porosity variations along the interface and subsequent flow localization.

V. CONCLUSIONS

In this work, we have investigated the effect of a coarse-fine grains interface on fluid ascent through water-saturated sands. The presence of dusts together with the fine grains in the top layer leads to flow self-organization and the formation of a regular fluidization pattern at the interface. We have quantified the pattern properties, with the following key results:

(1) A critical fluid velocity at the interface v_{ic} delimits the domains in which we observe either percolation in both layers ($v_i < v_{ic}$) or the formation of a quasiperiodic fluidization pattern right above the interface ($v_i > v_{ic}$).

(2) The pattern wavelength λ is roughly independent of the injected flow rate in the range of parameters explored in our experiments.

(3) λ is independent of the height of the top, fine grain layer.

(4) λ increases linearly with the coarse grain size d_c.

(5) Dusts present in the fine grain layer play a fundamental role. They infiltrate the coarse grain layer over a few coarse grain diameter beneath the interface. During fluid migration, they are entrained upward through the coarse grain pores and, due to local heterogeneities, trigger either pore clogging or neighboring flow focalization. Such an elutriation mechanism therefore leads to the formation of regular localized fluidized zones above the interface. A simple model based on the balance between vertical and horizontal pressure gradients right beneath the interface provides a prediction for the pattern wavelength $\lambda \sim \xi d_d (e/d_c)^{-1}$, with ξ a constant depending on the dusts penetration length, d_d the dust typical diameter, and (e/d_c) the typical number of coarse particles in the cell gap.

The fluidization pattern does not appear immediately when starting the fluid injection at the base of the coarse grains layer. Typically, the chimneys above the interface form after a transient ranging from below a second to a few seconds. Note that this transient time is much shorter than the time required for the incoming fluid to reach the interface. Among the many perspectives of this work, quantifying the transient regime leading to the pattern formation would be of interest to understand the mechanism at the grain scale leading to flow self-organization. However, such observations are difficult, if not impossible, experimentally and would require numerical simulations able to capture the dynamics at the pore scale.

Concerning applications, the formation of regular chimneys or pipes strongly resembles fluid seepage structures observed in sedimentary basins [10,12]. In such basins, geophysical acquisitions only provide a fixed image of fluid seep structures at a given time (the time of acquisition). It gives the envelope of a fluid pipe, and neither the internal architecture nor the volume of involved fluids (injected and expelled) has been characterized so far. Interpretations are based on the idea that each fluid pipe has a unique source at depth. In this work, we demonstrate that a unique injection point at depth may be the source of multiple fluid pipes and fluid seeps. Fluid seepage structures are usually encountered in an unconfined environment, which could make this conclusion open to debate, as the wavelength predicted by our model depends on

the confinement length e. Interestingly, natural fluid seepage also occurs in confined geometries such as seafloor gullies or steeply dipping fractures or faults, generating lined-up pockmarks (see Ref. [55], Fig. 6 and text within, among many other examples). Among the perspectives, the model could be adapted to an unconfined geometry by considering, for instance, a hexagonal lattice for the source distribution at the interface. This work is in progress as well as the setup of a three-dimensional experiment to investigate the possible appearance of a regular fluidization pattern in the laboratory. Another step will be to investigate multilayered granular systems, better representing the real geological millefeuille in nature.

ACKNOWLEDGMENTS

The authors thank G. Tangavelou for preliminary experiments during his internship in 2023, A. Burgisser for fruitful discussions which brought forth the elutriation process as the mechanism explaining the formation of the fluidization pattern, and S. Cola for introducing us to soil contact erosion. We are also grateful to two anonymous referees, whose comments greatly improved the manuscript.

DATA AVAILABILITY

The data that support the findings of this article are not publicly available upon publication because it is not technically feasible and/or the cost of preparing, depositing, and hosting the data would be prohibitive within the terms of this research project. The data are available from the authors upon reasonable request.

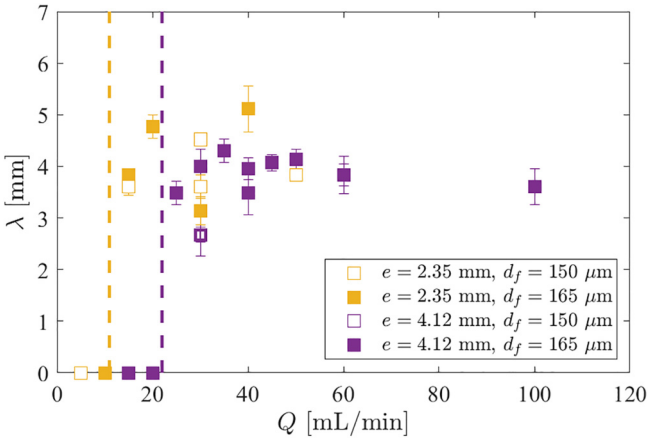

FIG. 10. Typical length λ of the fluidization pattern as a function of the injected flow rate Q. The vertical dashed lines indicate the critical flow rate Q_c, above which the fluidization pattern is observed for each cell gap e ($d_c = 750$ μm, $h_c = 8$ cm, and $h_f = 3$ cm).

APPENDIX: INFLUENCE OF THE INJECTION FLOW RATE Q

Figure 10 displays the dependence of λ with Q. The critical flow rate Q_c above which the fluidization pattern is observed depends on the cell gap e (Fig. 10, vertical dashed lines). Its value for $e = 4.12$ mm (dark purple) is about twice the value for the gap $e = 2.35$ mm (light orange). The flow rate is not the relevant parameter to collapse this transition (see Sec. III A).

[1] A. Gay and S. Migeon, Bull. Soc. Géol. France **188**, E3 (2017).
[2] V. Vidal and A. Gay, Pap. Phys. **14**, 140011 (2022).
[3] A. Carrara, A. Burgisser, and G. W. Bergantz, Earth Planet. Sci. Lett. **549**, 116539 (2020).
[4] A. Mazzini and G. Etiope, Earth-Sci. Rev. **168**, 81 (2017).
[5] A. L. Walters, J. C. Phillips, R. J. Brown, M. Field, T. Genon, G. Stripp, and R. S. J. Sparks, J. Volcanol. Geotherm. Res. **155**, 119 (2006).
[6] V. S. Stutkar, N. G. Deen, and J. A. M. Kuipers, Chem. Eng. Sci. **86**, 124 (2013).
[7] V. K. Jayaraman and B. D. Kulkarni, in *Chemical Engineering and Chemical Process Technology-Vol. III: Chemical Reaction Engineering*, edited by R. Pohorecki, J. Bridgwater, M. Molzahn, R. Gani, and C. Gallegos (EOLSS Publishers, United Kingdom, 2010), pp. 122–142.
[8] A. Nermoen, O. Galland, E. Jetestuen, K. Fristad, Y. Podladchikov, H. Svensen, and A. Malthe-Sørenssen, J. Geophys. Res. **115**, B10202 (2010).
[9] P. Philippe and M. Badiane, in *Advances in Bifurcation and Degradation in Geomaterials. Springer Series in Geomechanics and Geoengineering*, edited by S. Bonelli, C. Dascalu, and F. Nicot (Springer, Dordrecht, 2011), pp. 125–129.
[10] J. Cartwright and C. Santamarina, Mar. Pet. Geol. **65**, 126 (2015).
[11] L. Räss, N. S. C. Simon, and Y. Y. Podladchikov, Sci. Rep. **8**, 11116 (2018).
[12] A. Gay, G. Tangavelou, and V. Vidal, Fluids **9**, 66 (2024).
[13] T. Mörz, E. A. Karlik, S. Kreiter, and A. Kopf, Sediment. Geol. **196**, 251 (2007).
[14] G. Varas, V. Vidal, and J.-C. Géminard, Phys. Rev. E **83**, 011302 (2011).
[15] J. M. Link, L. A. Cuypers, N. G. Deen, and J. A. M. Kuipers, Chem. Eng. Sci. **60**, 3425 (2005).
[16] F. Zoueshtiagh and A. Merlen, Phys. Rev. E **75**, 056313 (2007).
[17] P. Philippe and M. Badiane, Phys. Rev. E **87**, 042206 (2013).
[18] S. E. Mena, L.-H. Luu, P. Cuéllar, P. Philippe, and J. S. Curtis, AIChE J. **63**, 1529 (2017).
[19] S. E. Mena, F. Brunier-Coulin, J. S. Curtis, and P. Philippe, Phys. Rev. E **98**, 042902 (2018).
[20] R. Mourgues, D. Bureau, L. Bodet, A. Gay, and J. B. Gressier, Earth Planet. Sci. Lett. **313-314**, 67 (2012).
[21] G. Varas, G. Ramos, J.-C. Géminard, and V. Vidal, Front. Phys. **3**, 44 (2015).
[22] M. Warsitzka, N. Kukowski, and F. May, Energy Procedia **114**, 3291 (2017).
[23] F. May, M. Warsitzka, and N. Kukowski, Int. J. Greenhouse Gas Control **90**, 102805 (2019).
[24] A. Farhat, P. Philippe, L.-H. Luu, A. Doghmane, and P. Cuéllar, Phys. Rev. Fluids **9**, 064305 (2024).

[25] G. Varas, G. Ramos, and V. Vidal, Phys. Rev. E **110**, 024901 (2024).
[26] Y.-F. Shi, Y. S. Yu, and L. T. Fan, Ind. Eng. Chem. Fund. **23**, 484 (1984).
[27] A. Mahadevan, A. V. Orpe, A. Kudrolli, and L. Mahadevan, Europhys. Lett. **98**, 58003 (2012).
[28] X. Cui, J. Li, A. Chan, and D. Chapman, Powder Technol. **254**, 299 (2014).
[29] E. P. Montellà, M. Toraldo, B. Chareyre, and L. Sibille, Phys. Rev. E **94**, 052905 (2016).
[30] J. Ngoma, P. Philippe, S. Bonelli, F. Radjaï, and J.-Y. Delenne, Phys. Rev. E **97**, 052902 (2018).
[31] A. Gay, R. Mourgues, C. Berndt, D. Burea, S. Planke, D. Laurent, S. Gautier, C. Lauer, and D. Loggia, Mar. Geol. **332-334**, 75 (2012).
[32] R. J. Nichols, R. S. J. Sparks, and C. J. N. Wilson, Sedimentology **41**, 233 (1994).
[33] V. M. Yarushina, L. H. Wang, D. Connolly, G. Kocsis, I. Faestø, S. Polteau, and A. Lakhlifi, Geology **50**, 179 (2022).
[34] See Supplemental Material at http://link.aps.org/supplemental/10.1103/2m8d-7h3j for a snapshot of Movie 1, where the injected water can be seen in blue. Note the quasiperiodic fluidization chimneys above the coarse/fine grains interface. The right image shows the zoom at the center (snapshot of Movie 2) ($e = 2.35$ mm, $d_c = 750$ μm, $h_c = 8$ cm, $d_f = 165$ μm, $h_f = 3$ cm, and $Q = 30$ mL/min). Movie 1 shows a typical experiment in real time. The movie starts exactly when the liquid injection starts ($t = 0$). Movie 2 has been acquired together with Movie 1, with another camera and lens magnifying a central area around the interface. Time in Movies 1 and 2 is synchronized. It shows the elutriation process in the coarse grain layer starting right at $t = 0$ and, after a short transient, the appearance of the fluidization chimneys.
[35] H. A. Janssen, Ver. Eutscher. Ing. Z. **39**, 1045 (1895).
[36] M. Sperl, Granular Matter **8**, 59 (2006).
[37] W. Snowsill, in *Instrumentation Reference Book*, 4th ed., edited by W. Boyes (Butterworth-Heinemann, Burlington, 2010), pp. 175–189.
[38] W.-C. Yang, in *Handbook of Fluidization and Fluid-Particle Systems*, edited by W.-C. Yang (CRC Press, Boca Raton, 2003), pp. 1–28.
[39] P. G. Saffman and G. I. Taylor, Proc. A **245**, 312 (1958).
[40] L. Rayleigh, Proc. London Math. Soc. **s1-14**, 170 (1883).
[41] G. I. Taylor, Proc. A **201**, 192 (1950).
[42] H. Geistlinger, G. Krauss, D. Lazik, and L. Luckner, Water Resour. Res. **42**, W07403 (2006).
[43] Ø. Johnsen, C. Chevalier, A. Lindner, R. Toussaint, E. Clément, K. J. Måløy, E. G. Flekkøy, and J. Schmittbuhl, Phys. Rev. E **78**, 051302 (2008).
[44] C. Chevalier, A. Lindner, M. Leroux, and E. Clément, J. Non-Newtonian Fluid Mech. **158**, 63 (2009).
[45] G. Varas, V. Vidal, and J.-C. Géminard, Phys. Rev. E **83**, 061302 (2011).
[46] R. Juanes, Y. Meng, and B. K. Primkulov, Phys. Rev. Fluids **5**, 110516 (2020).
[47] R. Beguin, Y.-H. Faure, C. Guidoux, and P. Philippe, *Scour and Erosion* (American Society of Civil Engineers, San Francisco, California, 2012), pp. 387–397.
[48] G. Cyril, F. Yves-Henri, R. Rémi, and H. Chia-Chun, J. Geotech. Geoenviron. Eng. **136**, 741 (2010).
[49] U.S. Army Corps of Engineers, *RMC Soil Contact Erosion (Initiation) Toolbox* (Dam and Levee Safety Programs, 2023).
[50] H. Yuan, A. Shapiro, Z. You, and A. Badalyan, Chem. Eng. J. **210**, 63 (2012).
[51] B. Muresan, N. Saiyouri, and P.-Y. Hicher, J. Environ. Eng. **139**, 692 (2013).
[52] M. M. Roozbahani and L. G.-B. an J. D. Frost, Int. J. Numer. Anal. Meth. Geomech. **38**, 1776 (2014).
[53] F. Núñez-González, J. P. Martín-Vide, and M. G. Kleinhans, Sedimentology **63**, 1209 (2016).
[54] J. E. Nielsen, D. Karup, L. W. de Jonge, M. Ahm, T. R. Bentzen, M. R. Rasmussen, and P. Moldrup, Soil Sci. Soc. Am. J. **82**, 1093 (2018).
[55] R. Jatiault, L. Loncke, D. Dhont, D. Dubucq, and P. Imbert, Mar. Pet. Geol. **103**, 773 (2019).